MOX-Report No. 104/2023

A computational model of the tumor microenvironment applied to fractionated radiotherapy

Possenti, L.; Gallo, A.; Vitullo, P.; Cicchetti, A.; Rancati, T.; Costantino, M.L.; Zunino, P.

MOX, Dipartimento di Matematica
Politecnico di Milano, Via Bonardi 9 - 20133 Milano (Italy)

mox-dmat@polimi.it https://mox.polimi.it

A computational model of the tumor microenvironment applied to fractionated radiotherapy

Luca Possenti, Andrea Gallo, Piermario Vitullo, Alessandro Cicchetti, Tiziana Rancati, Maria Laura Costantino and Paolo Zunino

Abstract Radiotherapy consists in delivering a precise radiation dose to a specific tumor target in order to eradicate tumor cells and to achieve local tumor control. The definition of the most suitable radiotherapy treatment schedule is not trivial due to the large tumor heterogeneity reported in clinical practice. The ultimate goal is to prescribe a specific treatment pattern for each patient, considering all the different radiobiological properties of the tumor / normal tissues to achieve the best final result possible. The model presented in this work goes in this direction, analyzing oxygen dependency and the role of the vascular network in the tumor microenvironment, since the efficacy of radiation therapy also depends on local oxygen availability. The

Luca Possenti
Fondazione IRCCS Istituto Nazionale dei Tumori, Milano, Italy, e-mail: luca.possenti@istitutotumori.mi.it

Andrea Gallo
Department of Chemistry, Materials and Chemical Engineering "Giulio Natta", Politecnico di Milano, Italy, e-mail: andrea5.gallo@mail.polimi.it

Piermario Vitullo
MOX, Department of Mathematics, Politecnico di Milano, Italy, e-mail: piermario.vitullo@polimi.it

Alessandro Cicchetti
Fondazione IRCCS Istituto Nazionale dei Tumori, Milano, Italy, e-mail: alessandro.cicchetti@istitutotumori.mi.it

Tiziana Rancati
Fondazione IRCCS Istituto Nazionale dei Tumori, Milano, Italy, e-mail: tiziana.rancati@istitutotumori.mi.it

Maria Laura Costantino
Department of Chemistry, Materials and Chemical Engineering "Giulio Natta", Politecnico di Milano, Italy, e-mail: marialaura.costantino@polimi.it

Paolo Zunino
MOX, Department of Mathematics, Politecnico di Milano, Italy, e-mail: paolo.zunino@polimi.it

main purpose of this work is to develop a mathematical model that describes the interaction between microvascular oxygen transfer and the efficacy of fractionated radiotherapy.

1 Introduction

Radiotherapy is recommended as part of treatment for more than 50% cancer patients [12]. It delivers a precise radiation dose to a specific tumor target to eradicate clonogenic (tumor) cells and achieve local tumor control. Identifying the most appropriate radiotherapy treatment schedule is not trivial due to the large tumor heterogeneity reported in clinical practice. Different tumor aggressiveness, tissue and tumor sensibility to radiation (i.e., radiosensitivity), and also possible microscopic / macroscopical tumor spread raise the level of complexity in radiotherapy treatment planning [5]. The ideal scenario would be the prescription of a specific treatment pattern for each patient, considering all radiobiological properties of the tumor / normal tissues and achieving the best final outcome possible. The model presented in this work moves exactly in this direction through the analysis of two specific factors that affect radiotherapy: oxygen dependency and the role of the vascular network.

Modern treatment planning guidelines in radiotherapy include dose fractionation [35], which consists of dividing the total dose into a set of daily dose fractions, with the purpose of minimizing side effects. The choice of the specific schedule (i.e., how many fractions, the amount of dose in each fraction, and the time gap between consecutive fractions) is driven by the radiobiological properties of the tumor and the normal tissues surrounding the target [8]. Normal tissue generally benefits from a high number of small-dose fractions, and tumors are somewhat less sensitive to fractionation.

Individual treatment planning and dose fractionation are determined by many factors, including those provided by radiobiological models, which describe the effect of radiation on cells and tissue [24]. When cells are irradiated, the integrity of the DNA structure is affected, and in some cases, huge modifications may appear in the genome. Radiation exposure can directly cause the rupture of chemical bonds that build up DNA or produce indirect damage by ionization of some molecules (e.g. water, with the formation of free radicals) that will enter in contact with DNA and cause chain breaks. At this level, the oxygen present in the vascular microenvironment plays a crucial role, stabilizing the radicals already formed, and thus securing the damage [9]. In case of low oxygen concentration, this process is impaired, leading to radioresistant behavior [14]. To evaluate the efficacy of radiotherapy, the concept of cell surviving fraction (SF) is commonly adopted, as it quantifies the proportion of cells that survive exposure to doses. Its value is a number in the range of 0 to 1, often expressed as a percentage. Different radiobiological models have been proposed to accurately predict SF before starting the radiotherapy treatment. Among them, the Linear-Quadratic (LQ) model is the gold standard, thanks to its simplicity and

prediction capabilities [26]. It assumes a proportionality between cell SF and the dose delivered, expressing the absorbed energy per unit mass of tissue (measured in Gray [Gy=J/Kg] in the SI system).

In this work, we consider a computational model to analyze the spatial distribution of the partial pressure of oxygen, or concentration, in the vascular microenvironment, deducing from different scenarios the importance of biological, mechanical and fluid parameters in the consequent hypoxia condition. Microvascular oxygen delivery is typically analyzed computationally, reducing the dimensionality of the vasculature by utilizing different methods. Models that account for the local morphology of the microvasculature have been developed recently, describing the microvasculature as a collection of localized sources, see for example [41] and more recently [13, 44]. This seminal idea has evolved into advanced multiphysics approaches [22, 33, 34], embracing vascular and interstitial flow, red blood cell transport, oxygen transport, angiogenesis, and enabling mesoscale analysis of the vascular microenvironment.

However, few of these models have been applied to study RT and tumor microenvironment. Scott and colleagues described the interaction between vascular density and a morphological index [40]. In a subsequent study, the same authors showed the importance of microvascular oxygen transport [11].

The main purpose of this work is to bridge the gap between advanced models of the vascular microenvironment and the application of radiobiological models to formulate fractionated radiotherapy plans. We achieve this goal using a mathematical model that describes the interaction between microvascular oxygen transfer and the efficacy of fractionated radiotherapy.

2 An oxygen transport model coupled to radiotherapy

In this section, partial differential equations (PDE) are used to model the physics of transport phenomena in the vascular microenvironment. Then the model is coupled with a radiobiological model to include the effect of radiotherapy.

2.1 A mixed-dimensional oxygen transport model

The mathematical framework of the vascular microenvironment is inherited from previous work by Possenti et al., where oxygen transport in a piece of tissue was modeled [32, 34]. In this chapter, the basic equations of the model are described in order to provide a context for the coupling with radiotherapy. The quantity of interest in this microcirculation problem is the oxygen concentration, transported both as free oxygen concentration (C) and bounded to hemoglobin ($CHbO_2$). Hemoglobin is a macromolecule incorporated in red blood cells (RBCs), which can chemically bond with oxygen molecules. In this way, oxygen is transported through the blood

vessel thanks to the red blood cells. Furthermore, oxygen could diffuse out of the RBC and then out of the vessel, crossing the vascular wall. For this reason, two regions are identified: Ω_t, corresponding to the tissue, and Ω_v, related to the vascular network (plasma and RBCs). The geometry of the vessels is reduced to a 1D object, identified by Λ [23, 34]. In the transport problem, oxygen concentration is treated as a function of both space and time: $C = C(x, t)$. Depending on the physical domain in which C is defined, a different notation is used for tissue or vessel. If the oxygen concentration in the tissue is considered, we use C_t and measure it using measured using ml_{O_2}/ml_{tissue}. On the contrary, the oxygen concentration in the vessel is indicated as C_v, where a different set of units is adopted, namely ml_{O_2}/ml_{blood}. Furthermore, two main assumptions are included, back from the previous work [34]:

- Steady state condition: the model does not consider time derivatives. It is reasonable to assume transport phenomena in microcirculation to occur in a slow-paced way, neglecting any transient variation to the physical quantities involved;
- Absence of body forces: no body forces (i.e. gravity, inertia) are included in this work.

We start with blood flow in the microvascular network. A mass balance is established for the transport of oxygen across the capillary membrane. In this scenario, it is important to note that oxygen is present as a free concentration as well as bound to hemoglobin $C_{tot} = C_v + C_{HbO_2}$, which must be considered. Moreover, two assumptions are required:

- Oxyhemoglobin cannot diffuse through the membrane: once the oxygen is bound to hemoglobin (inside RBC) the oxyhemoglobin molecule is successfully created. This molecule cannot diffuse outside the RBCs and therefore through the capillary membrane because of its large size;
- Temporal dynamics of oxygen diffusion through RBC is neglected: when oxygen leaves or enters the RBC, a diffusion process takes place. However, this kind of phenomenon is considered instantaneous in this framework, so it will not be relevant to the modeling.

Then, the general 3D transport equation of oxygen in the vessel could be written as:

$$\pi R^2 \, D_v \frac{\partial^2 C_v}{\partial s^2} - \pi R^2 \frac{\partial (u_v \, C_{tot})}{\partial s} = -J_{O_2}. \tag{1}$$

The main mechanisms that regulate oxygen transport in the tissue surrounding the vascular network are the following:

- Diffusion: this term describes oxygen diffusion in Ω_t. It is mainly governed by the diffusion coefficient D_t, expressed in m^2/s;
- Advection: it represents the motion of oxygen by convection, regulated by velocity u_t, expressed in m/s;

- Reaction: a sink term, illustrated by M, the consumption coefficient. It accounts for the amount of oxygen consumed by the tissue and is measured in $ml\,O_2/cm^3$.

Based on the aforementioned assumptions, the transport equation in the tissue reads:

$$\nabla \cdot (D_t \nabla(C_t)) - \nabla \cdot (\mathbf{u_t}\, C_t) + M\, C_t = J_{O_2} \quad \text{on } \Omega_t. \tag{2}$$

Finally, the oxygen transfer model is completed by describing the mechanisms that govern the tissue-vessel interaction. This model describes the total mass flow of oxygen J_{O_2}, which accounts for the sum of the diffusive mass flow (J_{diff}) and convective (J_{adv}) mass flow. Exploiting the theory of passive transport through semipermeable membranes, this term is modeled thanks to the Kedem-Katchalsky equation [17] as:

$$\begin{cases} J_{diff} = 2\pi R\, P_L (C_v - C_t) \\ J_{adv} = 2\pi R \left(\dfrac{C_v + C_t}{2} \right) L_p\, (\Delta P - \sigma \Delta \pi) \\ J_{O_2} = J_{diff} + J_{adv}, \end{cases} \tag{3}$$

where L_p is the hydraulic conductivity of the microvascular wall and π is the osmotic pressure and P_L is the vascular wall permeability to oxygen. We point out that, for small molecules, diffusion across the endothelial layer dominates greatly over transport. For example, using the parameters reported in Table 1 for oxygen, we see that the coefficient $2\pi R\, P_L$ of J_{diff} is four orders of magnitude higher than $2\pi R\, L_p$ appearing in J_{adv}. The second term on the right-hand side of (3) is important if the semi-permeable model is used for the transfer of large molecules, such as proteins, or to model very leaky vessels that can appear in the case of tumors.

2.2 Constitutive laws of the oxygen transport model

The model previously described is complemented by the following (non-linear) constitutive laws, namely, the Michaelis-Menten equation and the oxyhemoglobin concentration. The former describes the non-linear behavior of the oxygen consumption rate:

$$M(pO_2) = V_{max}\, \frac{pO_2}{pO_2 + P_{m_{50}}}, \tag{4}$$

where the consumption rate M is described as a function of oxygen partial pressure pO_2. The other two parameters are the maximum consumption rate in the tissue V_{max} ($mlO_2/cm^3/s$) and the partial pressure of oxygen at half the consumption rate $P_{m_{50}}$ ($mmHg$). Henry's law is applied ($C = \kappa P$), where a linear relationship between gas concentration and partial pressure is assumed. The linear parameter introduced (κ) represents the gas solubility in the environment and is a function of temperature

($\kappa = \kappa(T)$). So, Equation (4) is modified as:

$$M(C_{O_2}) = V_{max}\ \frac{C_{O_2}}{C_{O_2} + \kappa_t\ P_{m_{50}}}. \tag{5}$$

For V_{max} and $P_{m_{50}}$, physiological values from the literature will be adopted ($V_{max} = 6.17 \cdot 10^{-5}\ ml_{O_2}/cm^3/s$, $P_{m_{50}} = 1.0\ mmHg$) [33]. The oxygen solubility in the interstitium ($\kappa_t = 3.89 \cdot 10^{-5}\ ml_{O_2}/cm^3/mmHg$) is introduced and when coupled with $P_{m_{50}}$ gives rise to the Michaelis-Menten constant K_M ($= \kappa_t\ P_{m50}$).

The nonlinearity of the oxyhemoglobin concentration is described by the Hill equation to account for the saturation of RBC. In fact, the overall oxyhemoglobin concentration could be defined as $C_{HbO_2} = C_{Hb}\ S(pO_2)$ that involves the concentration of hemoglobin in the blood (C_{Hb}) and the saturation of hemoglobin within the RBC, named $S(pO_2)$. Furthermore, hemoglobin concentration depends on the binding capacity of heme groups N, the amount of hematocrit (H_t) in the blood (number of RBCs), and the Mean Corpuscular Hemoglobin Concentration ($MCHC$), representing the concentration of Hb in each RBC. As a result, we obtain $C_{Hb} = k_1\ H_t$, where $k_1 = N\ MCHC$. Oxygen saturation can be modeled using the Hill equation as follows:

$$S(pO_2) = \frac{pO_2^{\gamma}}{pO_2^{\gamma} + P_{s_{50}}^{\gamma}}. \tag{6}$$

The formulation is similar to the Michaelis-Menten formula (Eq. (4)), except for the Hill constant γ and $P_{s_{50}}$, the partial pressure of oxygen when hemoglobin reaches half saturation. Thus, applying Henry's law once again ($C = \kappa\ P$):

$$C_{HbO_2} = k_1 \cdot H_t \cdot \frac{C_{O_2}^{\gamma}}{C_{O_2}^{\gamma} + k_2^{\gamma}} \tag{7}$$

where $k_2 = (\kappa_{pl}\ P_{s_{50}})^{\gamma}$ is introduced to simplify the notation. Table 1 summarizes the values adopted in this work, obtained by fitting the Hill curve under physiological conditions [38].

Including the non-linear terms (Eq. (7) and Eq. (5)) in the transport problem (Eq. (2)), the overall system reads as follows:

$$\begin{cases} \nabla \cdot (D_t \nabla(C_t)) - \nabla \cdot (\mathbf{u_t}\ C_t) + V_{max}\ \dfrac{C_t}{C_t + K_M} = \\ 2\pi R\ [P_L(C_v - C_t) + \left(\dfrac{C_v + C_t}{2}\right) L_p\ (\Delta P - \sigma\Delta\pi)] \quad \text{on } \Omega_t \\ \\ \pi R^2\ D_v \dfrac{\partial^2 C_v}{\partial s^2} - \pi R^2 \dfrac{\partial(\mathbf{u_v}\ C_v)}{\partial s} - \pi R^2 \dfrac{\partial}{\partial s}\left(\mathbf{u_v}\ k_1\ H_t\ \dfrac{C_v^{\gamma}}{C_v^{\gamma} + k_2}\right) = \\ -2\pi R\ [P_L(C_v - C_t) + \left(\dfrac{C_v + C_t}{2}\right) L_p\ (1 - \sigma_{oxy})\ (\Delta P - \sigma\Delta\pi)] \quad \text{on } \Lambda. \end{cases} \tag{8}$$

2.3 The Linear-Quadratic radiobiological model

Radiotherapy consists in delivering a precise radiation dose to a specific tumor target in order to control the proliferation of clonogenic cells and possibly eradicate them. Evaluation of the cell death rate becomes crucial in this regard. Through clonogenic assays, for example, it is possible to quantify in-vitro the number of cells before and after radiation exposure, ensuring the clinical outcome prescribed by clinicians. To this purpose, the cell surviving fraction (SF) is evaluated, consisting of the proportion of cells that survive exposure to dose (i.e. cells that can still form colonies), usually computed as a percentage.

The eradication of cells described above is directly proportional to the total dose administered. Clinicians generally prescribe a sufficient dose to completely eradicate a tumor (SF close to 0), but the dose is typically not administered all at once. Indeed, the concept of fractionation is adopted, consisting of subdividing the dose into a set of dose fractions generally administered in time according to the radiobiological properties of the tumor and the surrounding tissues involved. The use of fractionation is justified by the 4R principle of radiobiology, demonstrating that splitting the dose into fractions brings benefits in terms of *repair, repopulation, redistribution, and reoxygenation* [28]. Tumors (and normal tissues) are dynamic elements constantly subjected to a very intense biological activity. Fractionation gives the possibility to normal tissue (slow proliferation, late responding cell) to repair part of the damage from one fraction to the next, while tumors (high proliferation, acute responding cells) are not affected by this process. Furthermore, improvement in terms of reoxygenation in tumors after every single fraction is related to vascular reorganization after vascular damage, enhancing oxygen redistribution in the tumor, and thus increasing the efficacy of radiotherapy in the next fraction. Due to these biological properties, an adequate and well-designed fractionation can widen the "therapeutic window", that is, increase the probability of eradicating the tumor without affecting the surrounding normal tissues [39].

The use of mathematical models in radiobiology has been well established since the past century, when the first type of model was developed to help investigators analyze and predict the effect of radiation exposure [4]. The Linear-Quadratic (LQ) model is the gold standard due to its simplicity and prediction capabilities. In this model, a lethal event in a single cell (single energy deposition causing a double-strand break in DNA) is taken into account by the linear term (α), whereas a sequence of multiple events causing a double-strand break (i.e. interaction of multiple radiation tracks) is demanded by the second-order term (β) [27]. The model was first described by Sinclair et al. in 1966 when the aim was to find a mathematical expression to fit the experimental data [43]; then Kellerer and Rossi (1971) formally derived the LQ model framework from the previous studies in single- and multihit models [18]. The formal equation of the LQ model is the following:

$$SF(D) = \exp(-\alpha D - \beta D^2). \tag{9}$$

This equation shows the surviving fraction (SF) as a function of the total dose provided (D) through some general parameters (α, β), representing the radiosensitivity of the tissue. The SF value is a number in the range of 0 to 1 (also expressed as a percentage) and is represented on a logarithmic scale. The formalism used is the standard, where a complete repair of sublethal damage between one fraction and the following is assumed. The linear parameter α $[Gy^{-1}]$ models the lethal damage provided to cells after one single hit, so it is linearly related to the dose. The quadratic parameter β $[Gy^{-2}]$ instead involves the accumulation of damage after multiple hits, proportional to the square of the dose administered. The value of these parameters depends on the ability of the tissue to resist radiation exposure, according to the type of cells involved and other tissue properties.

2.4 Coupling the oxygen transport and the radiobiological models

Describing the effect of radiotherapy on vascularized tissue is a very complex task [1, 45]. Radiation can start and accelerate atherosclerosis, leading to problems such as stroke and heart disease. In the tumor microenvironment, exposure to radiation has many effects: damage DNA, affect small blood vessels in both tumor and healthy tissue, and alter the way the immune system responds. Specifically, radiation harms endothelial cells (cells that line blood vessels). They become leaky, detach from their usual place, and can die. This dysfunction and cell death can cause inflammation, scarring, and blood clotting after radiation. Although changes caused by radiotherapy depend on the dose and type of radiation, predicting exactly how the TME will change is still a great challenge. Additionally, radiation can damage small blood vessels outside the tumor. The severity of the damage depends on the importance of the organ or system involved. Responses of normal tissues to radiation, both immediate and delayed, can limit the dose used in RT and affect the effectiveness of treatment and the patient's quality of life. It is vital to understand how radiation impacts small blood vessels in the tumor, but it has been difficult to study because of the challenges of watching how all these components respond together over time and in a living body. Traditional statistical models, which are heavily based on collecting a lot of data and finding associations between variables and outcomes, are not good at describing this complex environment. In conclusion, when considering vascular damage, its implications remain unclear, especially in a manner that facilitates integration within a model. Similarly, this claim is applicable to the remodeling of the vascular network. Currently, there is a paucity of data to elucidate how this occurs without resorting to substantial assumptions.

For these reasons, we present here a simplified model that accounts for the effect of radiotherapy on the vascular microenvironment, with the aim of coupling radiotherapy with oxygen transport. This model only addresses the effect of radiotherapy on the oxygen consumption rate, due to the variation in the number of cells in the tissue after radiotherapy. Therefore, we obtain different oxygen distributions at each fractionation step. In practice, we choose to modify the Michaelis-Menten formula

for oxygen consumption. Therefore, the reaction term is modified as shown:

$$M(C_t) = V_{max} \frac{C_t}{C_t + K_M} SF(C_t) \tag{10}$$

introducing a multiplication by the surviving fraction (SF). As the number of viable cells decreases during treatment, the consumption rate M also decreases, affecting the simulation of C_t. This effect is relevant only in the tissue domain (Ω_t), since, as discussed above, radiation damage to the vessels is not addressed in this work. Furthermore, we neglect the possible dynamic process of cell death (e.g., death via a later mitotic catastrophe), assuming that cell death occurs before the subsequent fraction.

To calculate SF we start from the classic linear-quadratic model (9). According to Wenzl and colleagues, α and β could be directly calculated, introducing the effect of the partial pressure of oxygen and the linear energy transfer parameter (LET), namely the amount of energy transferred per unit distance, depending on the type of radiation and its features [49, 50]. The radiosensitivity parameters are defined as,

$$\begin{cases} \alpha\ (pO_2, LET) = \dfrac{(a_1 + a_2\ LET) \cdot pO_2 + (a_3 + a_4\ LET) \cdot K}{pO_2 + K} \\ \sqrt{\beta\ (pO_2)} = \dfrac{b_1\ pO_2 + b_2\ K}{pO_2 + K} \end{cases} \tag{11}$$

where $a_1, a_2, a_3, a_4, b_1, b_2$ are parameters obtained by fitting *in vitro* data [49]. Instead, the coefficient K, is the oxygen tension at which the relative radiosensitivity reaches half of its maximum value and in this case is assumed equal to 2.5 mmHg [38]. As usual, each equation written in terms of oxygen partial pressure is rewritten as a function of the oxygen concentration thanks to the Henry's law ($pO_2\ (x) = C_t\ (x)/\kappa_t$). Thus, the surviving fraction reads as follows:

$$\begin{cases} SF\ (C_t) = exp\left(-\alpha(C_t)\ D - \beta(C_t)\ D^2\right) \\ \alpha\ (C_t, LET) = \dfrac{(a_1 + a_2\ LET) \cdot \dfrac{C_t}{\kappa_t} + (a_3 + a_4\ LET) \cdot K}{\dfrac{C_t}{\kappa_t} + K} \\ \sqrt{\beta\ (C_t)} = \dfrac{b_1\ \dfrac{C_t}{\kappa_t} + b_2\ K}{\dfrac{C_t}{\kappa_t} + K} \end{cases} \tag{12}$$

As mentioned above, fractionation consists of subdividing the total dose prescribed to the patient into smaller doses, called "fractions", in order to reduce normal tissue damage to the surroundings. To include the concept of fractionation, the fractiona-

tion index z is introduced. The fractionation index describes the distribution of dose fractions in the tumor and, therefore, the analysis of different fractionation patterns adopted by clinicians. The resulting SF will be evaluated fraction by fraction, summing the effect of those previously calculated. So, the fractionation index is defined as $z = 1, 2, 3, .., n_z$ ($z \in \mathbb{N}$), where n_z is the total number of fractions in which the total dose is subdivided. The counter on z progresses with the number of fractions effectively delivered. The fractionation index is initially set equal to 1 because at least one dose fraction is supposed to be released.

In this setting, the linear/quadratic model applied to a sequence of radiotherapy sessions, i.e. a fractionated treatment, is obtained from equation (12) as follows:

$$\begin{cases} SF^{(z)}\ (C_t) = SF^{(z-1)}\ exp\left[(-\alpha^{(z)}D - \beta^{(z)}D^2)\right] \\ \\ \alpha^{(z)}\ (C_t, LET) = \dfrac{(a_1 + a_2 LET) \cdot \dfrac{C_t^{(z-1)}}{\kappa_t} + (a_3 + a_4 LET) \cdot K}{\dfrac{C_t^{(z-1)}}{\kappa_t} + K} \\ \\ \sqrt{\beta^{(z)}\ (C_t)} = \dfrac{b_1 \dfrac{C_t^{(z-1)}}{\kappa_t} + b_2 K}{\dfrac{C_t^{(z-1)}}{\kappa_t} + K} \end{cases} \tag{13}$$

The transition between the previous radiation exposure, indicated as $z - 1$, and the current one, z, determines the dose accumulation process. Initial conditions are required to exploit the capability of the model fully:

- $SF^{(0)}$ must be set equal to 1 as it corresponds to the non-irradiation condition;
- $C_t^{(0)}$ corresponds to the oxygen distribution before the treatment starts. It is computed by assuming $SF^{(0)}$.

At this point, we are ready to couple the vascular microenvironment model with the one for fractionated radiotherapy. Starting from (8), we replace (10) with the original Michaelis-Menten term, $V_{max}\ \frac{C_t}{C_t + K_M}$. Then we express the survival fraction after each radiotherapy session as (13). In conclusion, the coupled model becomes:

$$
\begin{cases}
\nabla \cdot (D_t \nabla (C_t^{(z)})) - \nabla \cdot (\mathbf{u_t}\, C_t^{(z)}) + V_{max}\, \dfrac{C_t^{(z)}}{C_t^{(z)} + K_M}\, SF^{(z-1)} = \\
\qquad 2\pi R\, [P_L (C_v^{(z)} - C_t^{(z)}) \\
\qquad +(\dfrac{C_v^{(z)} + C_t^{(z)}}{2}) L_p\, (1 - \sigma_{oxy})\, (\Delta P - \sigma \Delta \pi)] \quad \text{on } \Omega_t \\
\pi R^2\, D_v \dfrac{\partial^2 C_v^{(z)}}{\partial s^2} - \pi R^2 \dfrac{\partial (\mathbf{u_v}\, C_v^{(z)})}{\partial s} - \pi R^2 \dfrac{\partial}{\partial s} (\mathbf{u_v}\, k_1\, H_t\, \dfrac{C_v^{(z),\gamma}}{C_v^{(z),\gamma} + k_2}) = \\
\qquad -2\pi R\, [P_L (C_v^{(z)} - C_t^{(z)}) \\
\qquad +(\dfrac{C_v^{(z)} + C_t^{(z)}}{2}) L_p\, (\Delta P - \sigma \Delta \pi)] \quad \text{on } \Lambda
\end{cases}
\tag{14}
$$

The model (14) represents a sequence of states of the vascular microenvironment during fractionated radiotherapy based on a quasi-static modeling approach. The simulation of a fractionated therapy requires an iterative process that describes how the tissue oxygenation and the survival fraction evolve from one fraction to the next one through the following steps:

- solve for the oxygen concentration in the tissue C_t and in the vessel C_v;
- update the value of SF, function of C_t obtained at the previous step;
- move to the next dose fraction, where SF will directly influence the oxygen distribution;
- back to the start till the end of the treatment.

2.5 Numerical methods

For complex geometrical configurations, explicit solutions of the oxygen transfer problem, namely problem (14), are not available. Numerical simulations are the only way to apply the model to real cases. The discretization of these models, described in [32], is achieved by the finite element method. Because of the particular mathematical structure of the model, based on mixed-dimensional differential equations, no commercially available simulator can handle it. All simulations have been performed using an internal C++ code based on the GetFem++ open source library [36].

The main advantage of the mixed-dimensional formulation adopted here is that the discretizations of the equations defined in the tissue and in the vascular network are completely independent in terms of the computational grids and the numerical schemes. We discretize the vascular network branches as separate subdomains. Each

of them is approximated by a piecewise straight line. The problems of blood flow and oxygen transfer are approximated using continuous piecewise-polynomial finite elements. The interstitial flow problem is approximated using mixed finite elements.

Because of the non-linear constitutive laws of the model, the problem formulated for each step of the sequence (14) has been further linearized by means of a fixed-point approach, and the solution of the coupled problem has been reached via an iterative process. At each iteration, the numerical discretization schemes described above provide a high-dimensional linear system of equations solved by means of state-of-the-art linear (iterative) solvers with suitable preconditioners. For further details on the computational methods, we refer to [23, 34].

The virtual tissue sample considered in this work consists of $500\,\mu m \times 500\,\mu m \times 500\mu m$ and has been discretized by means of a uniform tetrahedral mesh of 15 nodes on each side. Linear finite elements were used to perform the numerical discretization consisting of 4358 degrees of freedom (DOF). The discretization of the vascular network, instead, depends on the effective number of vessels introduced, precisely 28, 181, and 496 vessels, respectively, for the V2, V18, V36 (described below) corresponding to 560, 5021, and 9928 DOFs used for the discretization of each case. This numerical resolution has been considered satisfactory after a mesh-sensitivity analysis. In particular, the L^2-mean relative error in the approximation of oxygen concentration, C_t, between the considered mesh and a new lower resolution mesh (precisely $11 \times 11 \times 11$ points per side) was less than 1%.

3 Numerical simulations of the interaction of radiotherapy and the tumor microenvironment

In this section, we investigate the role of the tumor microenvironment in radiotherapy using the mathematical and computational tools presented before. We start by reporting in Table 1 the set of parameters used to initialize the model (14), except for some specific aspects related to radiobiological data that will be handled case by case. The sensitivity of the model on these parameters has recently been studied in [46].

A set of Voronoi capillary networks was inherited from previous work [32, 34], allowing simulations of different capillary densities. In fact, the blood network is crucial in defining the oxygen distribution within the tumor, leading to hypoxic or normoxic regions [46]. More precisely, we adopted three types of vascular networks:

- V2: low capillary density characterized by 28 capillaries;
- V18: high capillary density made up of 181 capillaries;
- V36: hyper-vascularized, consisting of 496 capillaries.

Parameter	Definition	Value	Ref.
D	Characteristic length of the problem	$5 \cdot 10^{-4}$ m	[34]
R	Average radius of the capillary	$4 \cdot 10^{-6}$ m	[34]
K	Tissue hydraulic conductivity	$3.6 \cdot 10^{-17}$ m^2	[42]
μ_t	Interstitial fluid viscosity	$1.2 \cdot 10^{-3}$ cP	[34]
μ_v	Blood viscosity	$3 \cdot 10^{-3}$ cP	[34]
L_p	Wall hydraulic conductivity	$1.4 \cdot 10^{-10}$ m^2 s kg^{-1}	[37]
π_v	Oncotic plasma pressure	2639.34 Pa	[15]
π_t	Oncotic interstitial pressure	1999.5 Pa	[44]
σ	Reflection coefficient	0.82	[42]
σ_{oxy}	Oxygen reflection coefficient	0.0	–
P_L	Permeability coefficient	$3.5 \cdot 10^{-5}$ m/s	[7],[22]
D_v	Diffusivity coefficient in vessels	$2.18 \cdot 10^{-9}$ m^2/s	[25]
D_t	Diffusivity coefficient in tissue	$2.41 \cdot 10^{-9}$ m^2/s	[25]
V_{max}	Oxygen consumption rate in tissue	$2.47 \cdot 10^{-4}$ $ml_{O_2}/cm^3/s$	[48]
C_{in}	Vessel inlet oxygen concentration	$3 \cdot 10^{-3}$ ml_{O_2}/ml_B	
N	Bound coefficient	1.36 ml_{O_2}/g_{Hb}	
γ	Hill constant	2.64 –	
$MCHC$	Hb concentration in RBC	0.34 g_{Hb}/ml_{RBC}	
$P_{s_{50}}$	pO_2 at half saturation	27 $mmHg$	

Table 1: *Set of parameters adopted to solve the oxygen transport model.*

For each of these networks, Murray's law was adopted to model the generation of the daughter vessel in the bifurcation process [34]. Furthermore, the ranges of capillary density considered were estimated based on the surface-to-volume ratio, namely the value of the lateral capillary surface over the volume of the tissue, precisely S/V = 10.19, 70.90, 144.16 mm^{-1} for cases V2, V18, V36 respectively.

We note that the virtual tissue sample of 500 μm × 500 μm × 500μm captures a small portion of any reasonably developed vascularized tumor. In these conditions, the variability of network structure and influence of the artificial boundaries may play a non-negligible role, also depending on the quantity of interest. The sensitivity of oxygen transfer to vascular density and distribution has been extensively discussed in [46], showing that for oxygenation the physical parameters (that is, those in Table 1 dominate over the variability of the vascular network. More precisely, C_{in} and V_{max} are the factors that influence primarily the mean value of the partial pressure in the tissue. Based on this evidence, we claim that the results presented in this work would not be significantly affected if a larger tissue sample were used, with a considerable increase in computational cost. To overcome this limitation, we have recently developed a surrogate model of (8) that takes advantage of deep learning-accelerated model order reduction techniques, enabling to solve the equations of the model in fraction of the time needed by the current approach [47].

3.1 The effect of fractionated radiotherapy

We study the effect of different fractionation patterns in order to maximize the effect of the total dose and simultaneously reduce the damage to normal tissue. New radiotherapy and online imaging technologies have allowed the spread of the so-called Stereotactic Body Radiation Therapy (SBRT) providing high doses (6-30 Gy) per fraction in a few fractions (1-8) [10, 29]. For this purpose, new ways of dose delivery have been proposed in recent years. A variety of dose patterns are generally reported in the literature, but there is a lack of agreement in the clinical radiobiology community on the optimum fractionation pattern. Thus, three radiotherapeutic patterns are considered here, from single-dose irradiation (1x48Gy) to more realistic hypofractionated patterns (4x12Gy, 6x8Gy) [3].

We simulate poorly perfused tissue characterized by the V2 network. The hypofractionation patterns performed were 1x48Gy, 4x12Gy, and 6x8Gy, displaying the same total dose (D_{tot} = 48 Gy) but released differently over time. Every fraction was delivered day by day, despite the large dose administered.

The main results of these simulations are shown in Figure 1. The non-homogeneity depicted in SF is affected by the low vascular density assumed in this case. It is a possible representation of tumor tissue, where hypoxic regions coexist with normoxic ones to create a heterogeneous distribution of oxygen. We note that in the single-fraction treatment, SF reaches values close to the minimum ($SF \approx 10^{-3}$) near the vessels, indicated by the green spots on the map. However, it should be noted that 1x48Gy is not a realistic treatment but a test case useful to make the comparison (30 Gy in 1 single fraction is the current "ceiling" used for very small tumors, [3]). For hypofractionated patterns, namely 4x12Gy and 6x8Gy, SF converges homogeneously to 10^{-3} at the end of the treatment (4° and 6° Fr, respectively) while the 1x48Gy case is only limited to an average of 10^{-1}, despite the large dose delivered all at once. This demonstrates that if a tumor is characterized by low oxygen supply due to insufficient vascularization, as exemplified by the case of the V2 Voronoi network, single dose irradiation is less effective in determining cell death compared to fractionated treatments as it does not take advantage of reoxygenation after radiotherapy, as will be extensively discussed in the following section.

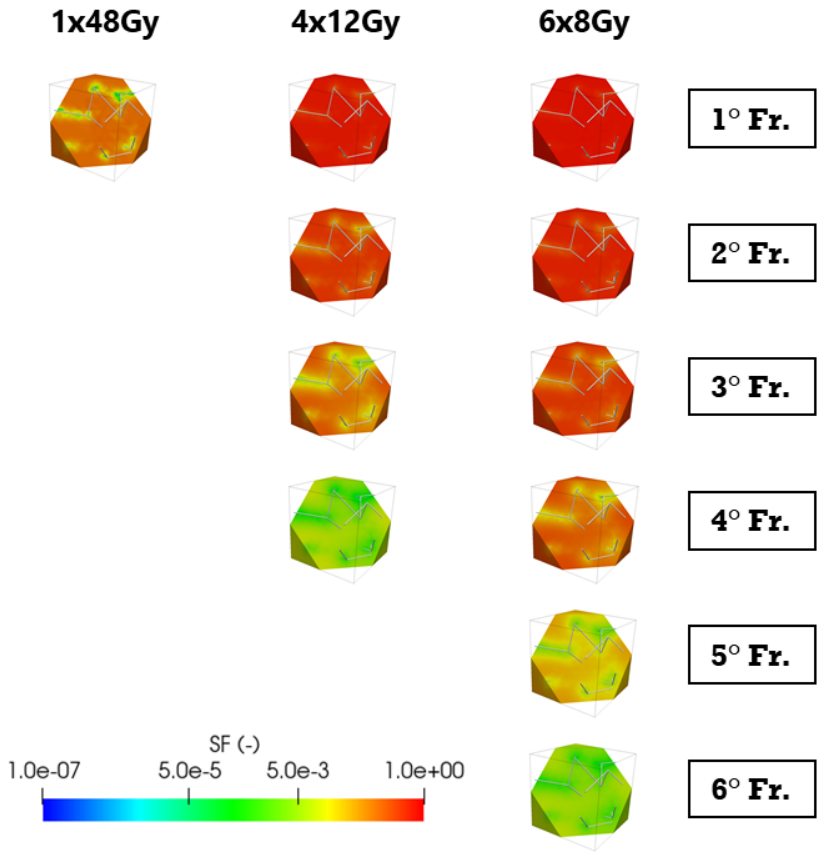

Fig. 1: *Surviving fraction distribution within tumor volume. Different fractionation patterns are reported to test the efficacy of hypofractionated radiotherapy.*

3.2 The effect of reoxygenation after radiotherapy

In this section, we compare the effect of radiotherapy on a set of different vascular networks, to account for the heterogeneity of tissue targets. In particular, Voronoi networks V2, V18, and V36 were used to simulate tumors (more precisely metastases) that occur in various biological structures.

It is well known that hypoxic regions are more resistant to radiation therapy than normoxic regions [9, 14], reducing the effect of radiation damage. Thus, tumor reoxygenation is one of the most important effects from a clinical point of view. It consists of improving tissue oxygenation in the tumor after each fraction of treatment. Hypoxic regions commonly arise in tumors, mainly due to the peculiar tumor

microvasculature that originates during the chaotic process of tumor angiogenesis. In fact, in a tumor vessel network, oxygen distribution is affected by defects in the vascular structure, such as dead ends, tortuous paths, and leaky walls. As a consequence, some parts of the tumor are not properly perfused, leading to hypoxic conditions.

Parameter	Definition	Value	Unit of measure	Ref.
a_1	Wenzl's parameter	0.15950134	$1/Gy$	-
a_2	Wenzl's parameter	0.00174001	$\mu m/(Gy \cdot keV)$	-
a_3	Wenzl's parameter	0.03625030	$1/Gy$	-
a_4	Wenzl's parameter	0.00224752	$\mu m/(Gy \cdot keV)$	-
b_1	Wenzl's parameter	0.09654740	$1/Gy$	-
b_2	Wenzl's parameter	0.00362053	$1/Gy$	-
LET	Linear energy transfer	2	$keV/\mu m$	[49],[50]
K	Wenzl's O_2 concentration	2.5	$mmHg$	[49],[50]

Table 2: *Radiobiological parameters for lung tumor.*

Table 2 reports the radiobiological data adopted for the tumor tissue. Here, Wenzl's parameters for the modified LQ model were adjusted to achieve the radiosensitivity properties of the lung, in particular, $\alpha = 0.16$ Gy^{-1} and $\alpha/\beta = 18$ Gy [19].

The relationship between oxygen distribution and the corresponding surviving fraction, intrinsically embedded in the radiobiological model, is depicted in Figure 2. The heterogeneity of $p\mathrm{O}_2$ distribution is based on the capillary network adopted, that is, V36, in this case. We observe that the central portion of the cubic domain is characterized by a larger $p\mathrm{O}_2$ (e.g. 65 mmHg) with respect to the periphery (e.g. 50 mmHg). As a consequence, the SF map resembles the oxygen one: portions characterized by high $p\mathrm{O}_2$ are inevitably more sensitive to radiation exposure, causing significant cell death, where SF reaches values close to 0.0430, meaning that less than 5% of cells survived treatment in the central portion. After radiation exposure, the new cell distribution affects $p\mathrm{O}_2$ in the next fraction, increasing the oxygen distribution in the central region, where a lower value of surviving cells was recorded. In addition, a more homogeneous oxygen pressure is generally achieved, reaching values around 76 mmHg.

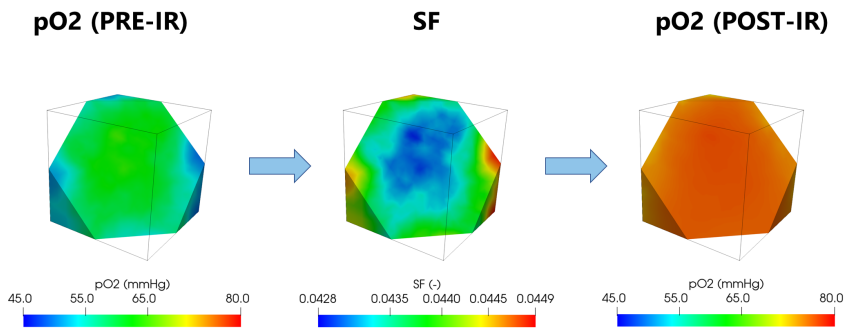

Fig. 2: *Local effect of oxygen pressure distribution on the surviving fraction of tumor cells. Before irradiation (IR), the central portion of the tumor is well-oxygenated, leading to significant cell death, as demonstrated by the vast blue area in SF. Finally, the pO_2 resulting after irradiation is depicted, where a more homogeneous oxygen distribution is present thanks to the reduction of available tumor cells.*

In Figure 3, we compare the effect of oxygenation on radiotherapy in three biological tissues with different vascular densities. Here, the same radiation pattern is provided in all the cases depicted, namely, a 4x12Gy, with the conventional one fraction per day, despite the high dose delivered.

A ripple effect is induced when the oxygen pressure varies within the treatment: the SF calculated for the previous fraction interacts with the oxygen consumption coefficient, modifying the amount of oxygen consumed by the cells. In this way, the consumption rate is reduced, leading to higher oxygen levels and a more uniform oxygen distribution in the tissue after radiotherapy.

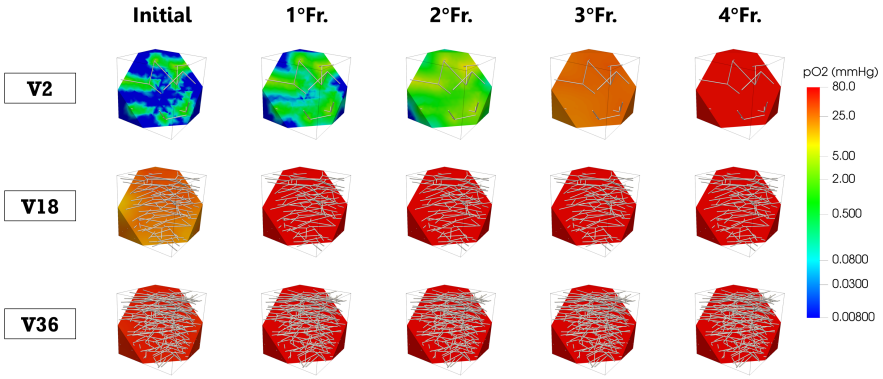

Fig. 3: *Evolution of oxygen partial pressure in tumor tissue according to the phase of radiotherapy cycle. A comparison among three types of vascular network is reported to emphasize the effect of reoxygenation with different initial oxygen distribution.*

An example of effective reoxygenation is reported in the case of low vascular density, namely V2, where tumor reoxygenation is crucial to achieving tumor control by radiotherapy. Initially, the oxygen distribution is poor in the tumor, limiting radiation damage. As the treatment progresses, radiotherapy reduces the number of surviving cells and thus prepares the environment for the next fraction. Therefore, oxygen could spread homogeneously within the tumor, reaching locations far from vessels. At the end of treatment, the tumor reaches a fully oxygenated state, with a mean value of 71.8 mmHg. In the V2 case, the effect of the initial distribution of oxygen is evident, especially in affecting inter-fractions variations, unlike what happens for V18 and V36, where a desired oxygen distribution is achieved after only one fraction. Indeed, the high vascular density of these two latter cases generates a uniform oxygen distribution from the beginning of treatment. In other words, radiotherapy is more effective if the tumor is fully oxygenated, as illustrated in Table 3.

	V2	**V18**	**V36**
SF_{Final}	$4.85 \cdot 10^{-3}$	$2.04 \cdot 10^{-5}$	$1.71 \cdot 10^{-5}$

Table 3: *Final value of SF in a 4x12Gy fractionation pattern considering the effect of the vascular network. A lower value of SF is observed for well-oxygenated conditions, namely V18 and V36.*

Another interesting aspect relies on the comparison of the oxygen distribution using different fractionation patterns on the same network (V2, in this case). The results confirmed that fractionated patterns improve oxygen distribution; see Figure 4. Indeed, the mean value of the partial oxygen pressure is 71.8 mmHg in the 6x8Gy pattern (blue line in the figure) and 71.0 mmHg in the case 4x12Gy (red). The path to reach the final point is different in the two cases, with the more fractionated therapy guaranteeing higher oxygenation throughout the treatment. Providing a low dose per day results in a less aggressive treatment that allows cell renewal and remodeling of the vasculature through which oxygen diffusion is enhanced. A slight difference is obtained between the two patterns in this scenario, since vasculature remodeling was not included. Since having large dose fractions, such as 12 Gy, may cause serious vascular damage, we expect a greater contribution of blood vessels in reoxygenation as the vascular response to irradiation is introduced. As a result, oxygen transport would be impaired.

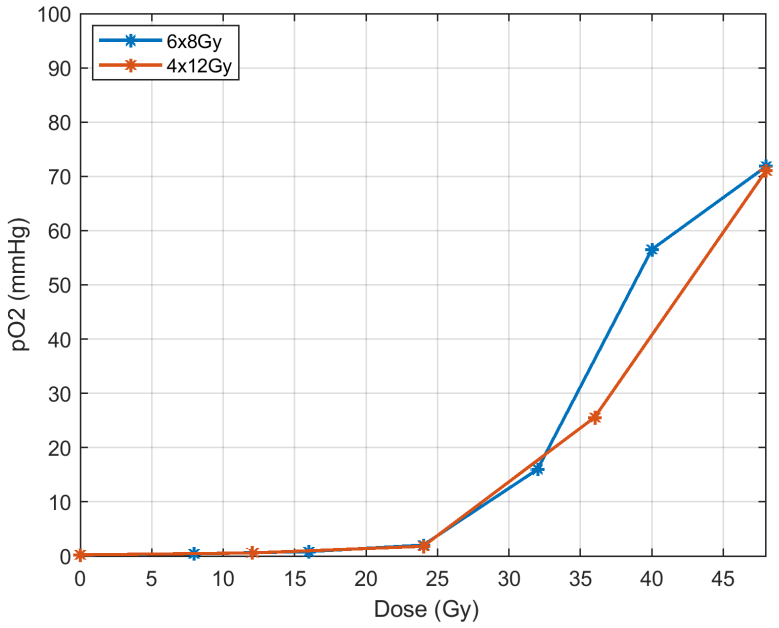

Fig. 4: *Comparison of pO_2 in 4x12Gy and 6x8Gy in lung tumors. Low-density vascular network, V2, was adopted to emphasize the differences in reoxygenation.*

3.3 The effect of vascular modifications due to radiotherapy

The impact of radiation on the microvasculature of a tumor is dose-dependent. High doses above 10 Gy can completely compromise the integrity of the vessel. Damage to the microvascular network can increase the number of hypoxic regions within the tumor. In these regions, the effectiveness of radiation therapy is further limited. The main effects of irradiation on blood vessels are mainly vascular collapse, degeneration of the vascular wall, and inflammation, increasing vascular leakage and permeability. Here, we focus mostly on the second factor, quantified as the increase in vascular permeability due to radiation therapy. The role of permeability is critical in defining the release of oxygen from vessels to tissue, as it determines whether substances can cross the endothelial barrier or not. In fact, a change in permeability has a pivotal effect, since a variation in oxygen concentration in the tissue greatly influences the effect of radiotherapy and the final clinical outcome.

A huge discrepancy has been observed in the variation of permeability following radiotherapy. Tumor heterogeneity is the main cause of this dispersion in the data. The size of the tumor, the type of cells irradiated, and the stage of the tumor are all elements that influence the surrounding microvasculature and thus the general

response to radiation. In particular, a general trend for increased vessel permeability is described in the literature immediately after irradiation. Table 4 provides an example of the variability of the data.

Dose	**Cells irradiated**	ΔP_L	**Ref.**
2 Gy	Primary HUVEC	+25%	[21]
4 Gy	Primary HUVEC	+35%	[21]
6x4.5 Gy	Imaging (NSCLC patients)	+8.4% (2°fr.), +44.8% (4°fr.), +20.5% (6°fr.)	[30]

Table 4: *Permeability variation following radiation exposure.*

Based on the aforementioned data, we assumed a permeability increase of + 35% following a photon-based single dose of 4 Gy, as reported in [21]. In particular, it was assumed that permeability would increase after each delivery. In addition, a dose-dependent behavior was included, as suggested in many works [2, 6, 16, 20, 31, 51]. We assumed a linear increase in the relationship between vessel permeability and the dose administered, given that a model for such a dose relationship is not defined.

The increase in permeability was simulated in a breast cancer environment, assuming $\alpha = 0.3$ Gy^{-1} and $\alpha/\beta = 3$ Gy. The total treatment time was 12 days, with the usual 5 fr/week pattern. The oxygen parameters were the same as previously used (see Table 1), with an initial value of vessel permeability $P_L = 3.5 \cdot 10^{-5}$ m/s. As an initial condition, we obtained the oxygen content provided by a V2 Voronoi network characterized by significant heterogeneity. The tumor was then irradiated with a dose fraction of 4 Gy, inducing a increase in permeability of + 35%. Moreover, a control case is illustrated, where the permeability was assumed constant throughout the treatment. Assuming a +35% increment, the value of permeability rises to $4.725 \cdot 10^{-5}$ m/s after the first fraction, leading to a local increase in the partial pressure of oxygen in the region surrounding the vessels (Fig. 5, 1 Fr.). Compared to the related control case, the higher partial oxygen pressure (green area) spreads out in the high-permeability case, achieving a more homogeneous oxygen distribution. This effect is emphasized during treatment, as shown in the 3° fraction, when the permeability (P_L) was $8.611 \cdot 10^{-5}$ m/s, confirming the trend previously described. More precisely, a mean pO_2 around 15 mmHg is achieved when assuming variation in permeability, while only 2 to 5 mmHg are present in the control case (Figure 5, 3°Fr.). The results demonstrate that the permeability increase during treatment generates better-oxygenated area all over the domain.

The results described above are the consequence of the positive superposition of the two effects, increased permeability, and decreased consumption. In fact, tissue oxygenation is facilitated by a decrease in the oxygen consumption rate, which is related to the death of tumor cells in the tissue. More precisely, greater radiation damage is induced in these regions because of the high oxygen content, leading to a lower surviving fraction. Consequently, treatment is more effective when permeability damage is considered, as demonstrated by the final value of SF we obtained

($SF_{control} = 1.34 \cdot 10^{-8}$; $SF_{\Delta P_L} = 1.65 \cdot 10^{-9}$). In particular, a lower value of 87% is recorded in SF when an increase in permeability 35% is considered.

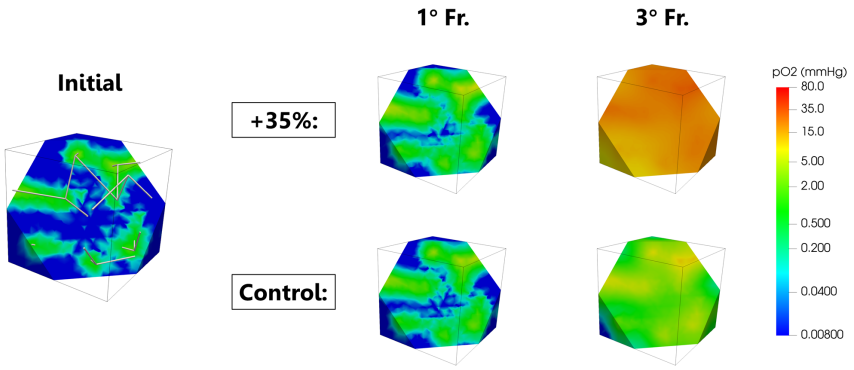

Fig. 5: *Effect of permeability variation in consecutive fractions. A comparison with a control case (constant permeability) is provided to appreciate the different oxygen distribution related to the permeability increment.*

Finally, the variation in oxygen pressure throughout treatment is investigated in Fig. 6. As usual, the mean value of pO_2 in the tumor tissue is reported in each fraction. Assuming an increase in vessel permeability, a higher value of mean oxygen pressure is expected within a few fractions. Therefore, in the case of +35% and +52.5% increment, the pO_2 curve shifts towards the left, reaching the maximum level of oxygenation before the control curve (constant permeability). This confirms the previously shown results, where oxygenation is enhanced because of increased permeability. However, as soon as the maximum is reached, the + 35% and +52.5% curves suddenly decrease, despite the constant increase in permeability. This peculiar phenomenon can be explained from a mathematical point of view. In fact, equilibrium is reached in terms of oxygen concentration between blood vessels (C_v) and tumor tissue (C_t) as permeability increases since oxygen diffuses from the higher to the lower concentrated districts until a concentration gradient is available. As a consequence, the term $(C_v - C_t)$ of equation (8), which involves oxygen transport through the vessel barrier, is rapidly reduced during the fractionation process, affecting the variation of oxygen concentration (C_t) in the following fraction. In other words, the constant increase in permeability is balanced by a decrease in the transmural concentration gradient. In this way, the oxygen support to the tissue decreases, while the oxygen consumption rate remains unchanged. The combination of these effects explains the slight decrease in oxygen levels in the case of highly permeable vessels. Instead, for the control curve, no significant variations are reported. The constant permeability maintains equilibrium without involving any variation in C_t.

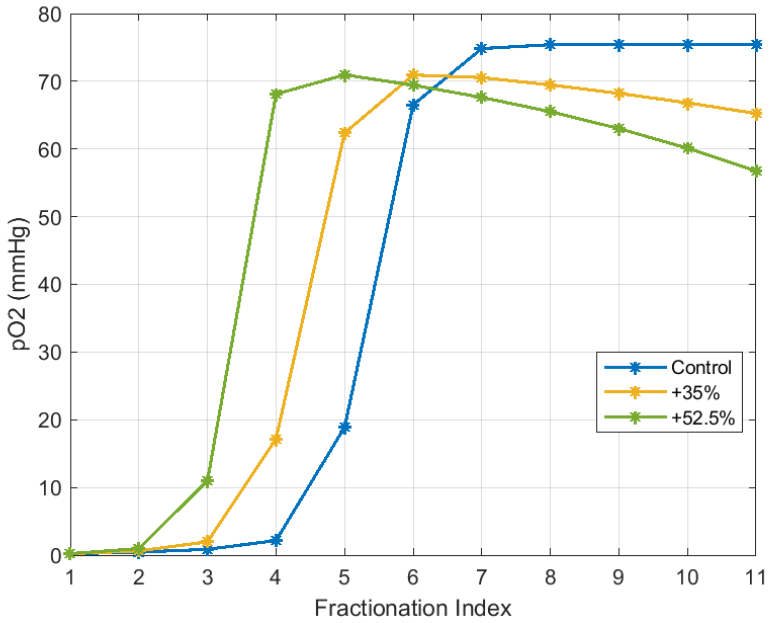

Fig. 6: *Mean oxygen pressure for different fractions of the treatment. Increasing the dose per fraction has a significant effect on nominal permeability variation, resulting in an enhancement of the oxygenation process. Indeed, the maximum point is reached in fewer fractions in the +52.5% case (green curve) as compared to the +35% one (yellow curve).*

4 Discussion and conclusions

In this work, we study the effect of oxygen concentration in radiotherapy through the coupling of a radiobiological model with an oxygen transport model in the vascular microenvironment. First, the Linear-Quadratic radiobiological model was modified to include the dependence on the partial pressure of oxygen, as proposed by Wenzl et al. [49, 50]. This allows us to relate the surviving fraction with the amount of oxygen available through the tumor radiobiological properties α and β. Second, the radiobiological model was incorporated into a sophisticated oxygen transport model, where the oxygen exchange in the microvascular environment was simulated. A numerical approach was adopted to solve the complex system of equations resulting from the above-mentioned coupling.

The proposed model was particularly useful for the analysis of the phenomenon of reoxygenation in the tumor microenvironment. During treatment, radiation therapy progressively reduced the number of viable tumor cells, affecting oxygen consump-

tion in the tumor. As a result, an increase in oxygenation is observed, assuming a constant blood washout between consecutive fractions. As a limitation of the model, tumor reoxygenation may also include other aspects related to the tumor microenvironment, such as vascular remodeling. Rearrangement of the microvascular network after radiotherapy greatly affects oxygen redistribution and should therefore be included in this model.

In terms of the study of the permeability variation, instead, we remark on the important simplifications adopted to model the dose-dependent behavior. The results show that the increase in permeability enhances reoxygenation, but we assume a linear relationship is assumed between the increase in permeability and the dose per fraction delivered. More research is required to model the dose-dependent effect on permeability. Also, due to vascular damage, an abnormal increase in permeability is probably related to a rise in interstitial fluid pressure and undesired extravasation of large molecules (advective phenomena), causing vessel collapse and thus decreasing blood vessel density in the tumor.

Simulated treatments show, on average, good efficacy in tumor eradication, quantified by the low value achieved in the surviving fraction (SF). Compared to clinical observations, these results look quite optimistic. Tumor recurrence remains a problem, despite the simulations performed and the related promising results. This discrepancy between simulations and reality may be explained by observing that we have modeled a well-oxygenated tumor environment characterized by a homogeneous distribution of oxygen partial pressure that explains such optimistic results in survival fraction after radiotherapy. In fact, a limitation of this work consists in considering a rather small sample describing a well-perfused microenvironment characterized by a regular and organized vascular network, generally not observed in tumors. This limitation was partially overcome by simulating vascular networks with low vascular density. As expected, hypofractionated patterns showed low performance in this case due to the poor reoxygenation that induces a hyperradioresistant response.

In addition to that, this work supports the importance of oxygenation and its changes in the framework of radiation therapy, and the proposed model can be used to analyze the tumor microenvironment during fractionated radiotherapy.

Acknowledgement

Paolo Zunino acknowledges the support of the grant MUR PRIN 2022 No. 2022WKWZA8 *Immersed methods for multiscale and multiphysics problems* (IMMEDIATE). The present research is part of the activities of the Dipartimento di Eccellenza 2023-2027 project, funded by MUR. Piermario Vitullo and Paolo Zunino are members of the Gruppo Nazionale per il Calcolo Scientifico (GNCS), Istituto Nazionale di Alta Matematica (INdAM).

References

[1] Baker, D.G., Krochak, R.J.: The response of the microvascular system to radiation: A review. Cancer Investigation **7**(3), 287–294 (1989). DOI 10.3109/07357908909039849

[2] Barker, H.E., Paget, J.T.E., Khan, A.A., Harrington, K.J.: The tumour microenvironment after radiotherapy: mechanisms of resistance and recurrence. Nature Reviews Cancer **15**, 409–425 (2015)

[3] Bedard, G., McDonald, R., Poon, I., Erler, D., Soliman, H., Cheung, P., Chung, H., Chu, W., Loblaw, A., Chow, E., Sahgal, A.: Stereotactic body radiation therapy for non-spine bone metastases–a review of the literature. Annals of palliative medicine **5**, 58–66 (2016). DOI 10.3978/j.issn.2224-5820.2015.07.01

[4] Brenner, D.J., Hlatky, L.R., Hahnfeldt, P.J., Huang, Y., Sachs, R.K.: The linear-quadratic model and most other common radiobiological models result in similar predictions of time-dose relationships. Radiation research **150**, 83–91 (1998)

[5] Buffa, F.M.: Fundamental radiobiology and its application to radiation oncology. In: Y. Lemoigne, A. Caner (eds.) Radiotherapy and Brachytherapy, pp. 3–9. Springer Netherlands, Dordrecht (2009)

[6] Castle, K.D., G, K.D.: Establishing the impact of vascular damage on tumor response to high-dose radiation therapy. Cancer Research **79**, 5685–5692 (2019)

[7] Cattaneo, L., Zunino, P.: A computational model of drug delivery through microcirculation to compare different tumor treatments. International Journal for Numerical Methods in Biomedical Engineering **30**(11), 1347–1371 (2014)

[8] De Ruysscher, D., Niedermann, G., Burnet, N., Siva, S., Lee, A., Hegi-Johnson, F.: Radiotherapy toxicity. Nature Reviews Disease Primers **5**(1) (2019)

[9] Eui Jung Moon, K.P., Olcina, M.M.: The importance of hypoxia in radiotherapy for the immune response, metastatic potential and flash-rt. International Journal of Radiation Biology **98**(3), 439–451 (2022). DOI 10.1080/09553002.2021.1988178

[10] Grimm, J., Marks, L.B., Jackson, A., Kavanagh, B.D., Xue, J., Yorke, E.: High dose per fraction, hypofractionated treatment effects in the clinic (hytec): An overview. International Journal of Radiation Oncology*Biology*Physics **110**, 1–10 (2021). DOI 10.1016/j.ijrobp.2020.10.039

[11] Grogan, J.A., Markelc, B., Connor, A.J., Muschel, R.J., Pitt-Francis, J.M., Maini, P.K., Byrne, H.M.: Predicting the influence of microvascular structure on tumor response to radiotherapy. IEEE Transactions on Biomedical Engineering **64**, 504–511 (2017)

[12] Hanna, T.P., King, W.D., Thibodeau, S., Jalink, M., Paulin, G.A., Harvey-Jones, E., O'Sullivan, D.E., Booth, C.M., Sullivan, R., Aggarwal, A.: Mortality due to cancer treatment delay: systematic review and meta-analysis. BMJ **371** (2020). DOI 10.1136/bmj.m4087

[13] Hartung, G., Badr, S., Moeini, M., Lesage, F., Kleinfeld, D., Alaraj, A., Linninger, A.: Voxelized simulation of cerebral oxygen perfusion elucidates hypoxia in aged mouse cortex. PLOS Computational Biology **17**, e1008584 (2021)

[14] Horsman, M.R., Mortensen, L.S., Petersen, J.B., Busk, M., Overgaard, J.: Imaging hypoxia to improve radiotherapy outcome. Nature Reviews Clinical Oncology **9**, 674–687 (2012)

[15] Jain, R.K., Tong, R.T., Munn, L.L.: Effect of vascular normalization by antiangiogenic therapy on interstitial hypertension, peritumor edema, and lymphatic metastasis: Insights from a mathematical model. Cancer Research **67**, 2729–2735 (2007)

[16] Jarosz-Biej, M., Smolarczyk, R., Cichoń, T., Kułach, N.: Tumor microenvironment as a "game changer" in cancer radiotherapy. International Journal of Molecular Sciences **20**, 3212 (2019)

[17] Jarzyńska, M.: The application of practical kedem-katchalsky equations in membrane transport. Open Physics **4**, 429–438 (2006)

[18] Kellerer, A.M., Rossi, H.H.: Rbe and the primary mechanism of radiation action. Radiation research **47**, 15–34 (1971)

[19] Klement, R.J.: Radiobiological parameters of liver and lung metastases derived from tumor control data of 3719 metastases. Radiotherapy and Oncology **123**, 218–226 (2017)

[20] Kocher, M., Treuer, H., Voges, J., Hoevels, M., Sturm, V., Müller, R.P.: Computer simulation of cytotoxic and vascular effects of radiosurgery in solid and necrotic brain metastases. Radiotherapy and Oncology **54**, 149–156 (2000)

[21] Kouam, P.N., Rezniczek, G.A., Adamietz, I.A., Bühler, H.: Ionizing radiation increases the endothelial permeability and the transendothelial migration of tumor cells through adam10-activation and subsequent degradation of vecadherin. BMC Cancer **19**, 958 (2019)

[22] Köppl, T., Vidotto, E., Wohlmuth, B.: A 3d-1d coupled blood flow and oxygen transport model to generate microvascular networks. International Journal for Numerical Methods in Biomedical Engineering **36** (2020)

[23] Laurino, F., Zunino, P.: Derivation and analysis of coupled pdes on manifolds with high dimensionality gap arising from topological model reduction. ESAIM: M2AN **53**(6), 2047–2080 (2019)

[24] van Leeuwen, C.M., Oei, A.L., Crezee, J., Bel, A., Franken, N.A.P., Stalpers, L.J.A., Kok, H.P.: The alfa and beta of tumours: a review of parameters of the linear-quadratic model, derived from clinical radiotherapy studies. Radiation Oncology **13**(1), 96 (2018). DOI 10.1186/s13014-018-1040-z

[25] Lücker, A., Weber, B., Jenny, P.: A dynamic model of oxygen transport from capillaries to tissue with moving red blood cells. American Journal of Physiology-Heart and Circulatory Physiology **308**, H206–H216 (2015)

[26] McMahon, S.: The linear quadratic model: Usage, interpretation and challenges. Physics in Medicine and Biology **64**(1) (2019)

[27] McMahon, S.J.: The linear quadratic model: usage, interpretation and challenges. Physics in Medicine & Biology **64**, 01TR01 (2018)

[28] McMahon, S.J., Prise, K.M.: Mechanistic modelling of radiation responses. Cancers **11**, 205 (2019)

[29] Navarria, P., Baldaccini, D., Clerici, E., Marini, B., Cozzi, L., Franceschini, D., Bertuzzi, A.F., Quagliuolo, V., Torri, V., Colombo, P., Franzese, C., Bellu, L., Scorsetti, M.: Stereotactic body radiation therapy for lung metastases from sarcoma in oligometastatic patients: A phase 2 study. International Journal of Radiation Oncology*Biology*Physics **114**, 762–770 (2022). DOI 10.1016/j.ijrobp.2022.08.028

[30] Ng, Q.S., Goh, V., Milner, J., Padhani, A.R., Saunders, M.I., Hoskin, P.J.: Acute tumor vascular effects following fractionated radiotherapy in human lung cancer: In vivo whole tumor assessment using volumetric perfusion computed tomography. International Journal of Radiation Oncology*Biology*Physics **67**, 417–424 (2007)

[31] Park, H.J., Griffin, R.J., Hui, S., Levitt, S.H., Song, C.W.: Radiation-induced vascular damage in tumors: Implications of vascular damage in ablative hypofractionated radiotherapy (sbrt and srs). Radiation Research **177**, 311–327 (2012)

[32] Possenti, L., Casagrande, G., Di Gregorio, S., Zunino, P., Costantino, M.: Numerical simulations of the microvascular fluid balance with a non-linear model of the lymphatic system. Microvascular Research **122**, 101–110 (2019)

[33] Possenti, L., Cicchetti, A., Rosati, R., Cerroni, D., Costantino, M.L., Rancati, T., Zunino, P.: A mesoscale computational model for microvascular oxygen transfer. Annals of Biomedical Engineering (2021)

[34] Possenti, L., di Gregorio, S., Gerosa, F., Raimondi, G., Casagrande, G., Costantino, M., Zunino, P.: A computational model for microcirculation including fahraeus-lindqvist effect, plasma skimming and fluid exchange with the tissue interstitium. International Journal for Numerical Methods in Biomedical Engineering **35**(3) (2019)

[35] Ratosa, I., Jenko, A., Oblak, I.: Breast size impact on adjuvant radiotherapy adverse effects and dose parameters in treatment planning. Radiology and Oncology **52**(3), 233–244 (2018). DOI doi:10.2478/raon-2018-0026

[36] Renard, Y., Poulios, K.: Getfem: Automated fe modeling of multiphysics problems based on a genericweak form language. ACM Transactions on Mathematical Software **47**(1) (2021)

[37] Rippe, B., Kamiya, A., Folkow, B.: Simultaneous measurements of capillary diffusion and filtration exchange during shifts in filtration-absorption and at graded alterations in the capillary permeability surface area product (ps). Acta Physiologica Scandinavica **104**, 318–336 (1978)

[38] Rosati, R.: A multi-scale computational model for micro-vascular oxygen transfer applied to radiotherapy (2019)

[39] Santiago, A., Barczyk, S., Jelen, U., Engenhart-Cabillic, R., Wittig, A.: Challenges in radiobiological modeling: can we decide between lq and lq-l models based on reviewed clinical nsclc treatment outcome data? Radiation Oncology **11**, 67 (2016)

[40] Scott, J.G., Fletcher, A.G., Anderson, A.R.A., Maini, P.K.: Spatial metrics of tumour vascular organisation predict radiation efficacy in a computational model. PLOS Computational Biology **12**, e1004712 (2016)

[41] Secomb, T., Hsu, R., Park, E., Dewhirst, M.: Green's function methods for analysis of oxygen delivery to tissue by microvascular networks. Annals of Biomedical Engineering **32**(11), 1519–1529 (2004)

[42] Sefidgar, M., Soltani, M., Raahemifar, K., Sadeghi, M., Bazmara, H., Bazargan, M., Naeenian, M.M.: Numerical modeling of drug delivery in a dynamic solid tumor microvasculature. Microvascular Research **99**, 43–56 (2015)

[43] Sinclair, W.: The shape of radiation survival curves of mammalian cells cultured in vitro (1966)

[44] Sweeney, P., D'esposito, A., Walker-Samuel, S., Shipley, R.: Modelling the transport of fluid through heterogeneous, whole tumours in silico. PLoS Computational Biology **15**(6) (2019)

[45] Venkatesulu, B.P., Mahadevan, L.S., Aliru, M.L., Yang, X., Bodd, M.H., Singh, P.K., Yusuf, S.W., ichi Abe, J., Krishnan, S.: Radiation-induced endothelial vascular injury: A review of possible mechanisms. JACC: Basic to Translational Science **3**(4), 563–572 (2018). DOI https://doi.org/10.1016/j.jacbts.2018.01.014

[46] Vitullo, P., Cicci, L., Possenti, L., Coclite, A., Costantino, M.L., Zunino, P.: Sensitivity analysis of a multi-physics model for the vascular microenvironment. International Journal for Numerical Methods in Biomedical Engineering **n/a**(n/a), e3752 (2023). DOI https://doi.org/10.1002/cnm.3752

[47] Vitullo, P., Colombo, A., Franco, N.R., Manzoni, A., Zunino, P.: Nonlinear model order reduction for problems with microstructure using mesh informed neural networks. to appear on Finite Elements in Analysis Design (2023). ArXiv:2309.07815

[48] Welter, M., Fredrich, T., Rinneberg, H., Rieger, H.: Computational model for tumor oxygenation applied to clinical data on breast tumor hemoglobin concentrations suggests vascular dilatation and compression. PLOS ONE **11**, e0161267 (2016)

[49] Wenzl, T., Wilkens, J.J.: Modelling of the oxygen enhancement ratio for ion beam radiation therapy. Physics in Medicine and Biology **56**, 3251–3268 (2011)

[50] Wenzl, T., Wilkens, J.J.: Theoretical analysis of the dose dependence of the oxygen enhancement ratio and its relevance for clinical applications. Radiation Oncology **6**, 171 (2011)

[51] Wijerathne, H., Langston, J.C., Yang, Q., Sun, S., Miyamoto, C., Kilpatrick, L.E., Kiani, M.F.: Mechanisms of radiation-induced endothelium damage: Emerging models and technologies. Radiotherapy and Oncology **158**, 21–32 (2021)

MOX Technical Reports, last issues

Dipartimento di Matematica
Politecnico di Milano, Via Bonardi 9 - 20133 Milano (Italy)

103/2023 Dimola N.; Kuchta M.; Mardal K.A.; Zunino P.
Robust Preconditioning of Mixed-Dimensional PDEs on 3d-1d domains coupled with Lagrange Multipliers

101/2023 Formaggia, L.; Zunino, P.
Hybrid dimensional models for blood flow and mass transport

98/2023 Lespagnol, F.; Grandmont, C.; Zunino, P.; Fernandez, M.A.
A mixed-dimensional formulation for the simulation of slender structures immersed in an incompressible flow

100/2023 Vitullo, P.; Cicci, L.; Possenti, L.; Coclite, A.; Costantino, M.L.; Zunino, P.
Sensitivity analysis of a multi-physics model for the vascular microenvironment

96/2023 Bonetti, S.; Botti, M.; Antonietti, P.F.
Robust discontinuous Galerkin-based scheme for the fully-coupled non-linear thermo-hydro-mechanical problem

95/2023 Barnafi, N. A.; Regazzoni, F.; Riccobelli, D.
Reconstructing relaxed configurations in elastic bodies: mathematical formulation and numerical methods for cardiac modeling

93/2023 Andrini, D.; Magri, M.; Ciarletta, P.
Optimal surface clothing with elastic nets

92/2023 Burzacchi, A.; Rossi, L.; Agasisti, T.; Paganoni, A. M.; Vantini, S.
Commuting time as a determinant of higher education students' performance: the case of Politecnico di Milano

Burzacchi, A.; Rossi, L.; Agasisti, T.; Paganoni, A. M.; Vantini, S.
Commuting time as a determinant of higher education students' performance: the case of Politecnico di Milano

90/2023 Gregorio, C.; Baj, G.; Barbati, G.; Ieva, F.
Dynamic treatment effect phenotyping through functional survival analysis